



Intermittency and Ion Temperature–Anisotropy Instabilities: Simulation and Magnetosheath Observation

Ramiz A. Qudsi¹ , Riddhi Bandyopadhyay¹ , Bennett A. Maruca^{1,2} , Tulasi N. Parashar^{1,3} , William H. Matthaeus^{1,2} , Alexandros Chasapis⁴ , S. Peter Gary⁵ , Barbara L. Giles⁶ , Daniel J. Gershman⁶ , Craig J. Pollock⁷ , Robert J. Strangeway⁸ , Roy B. Torbert⁹ , Thomas E. Moore⁶ , and James L. Burch¹⁰

¹ Department of Physics and Astronomy, University of Delaware, Newark, DE 19716, USA

² Bartol Research Institute, Newark, DE, USA

³ School of Chemical and Physical Science, Victoria University of Wellington, Kelburn, Wellington 6012, New Zealand

⁴ Laboratory for Atmospheric and Space Physics, University of Colorado Boulder, Boulder, CO, USA

⁵ Space Science Institute, Boulder, CO, USA

⁶ NASA Goddard Space Flight Center, Greenbelt, MD 20771, USA

⁷ Denali Scientific, Fairbanks, AK 99709, USA

⁸ University of California, Los Angeles, CA 90095-1567, USA

⁹ University of New Hampshire, Durham, NH 03824, USA

¹⁰ Southwest Research Institute, San Antonio, TX 78238-5166, USA

Received 2020 February 17; revised 2020 April 13; accepted 2020 April 14; published 2020 May 28

Abstract

Weakly collisional space plasmas are rarely in local thermal equilibrium and often exhibit non-Maxwellian electron and ion velocity distributions that lead to the growth of microinstabilities—that is, enhanced electric and magnetic fields at relatively short wavelengths. These instabilities play an active role in the evolution of space plasmas, as does ubiquitous broadband turbulence induced by turbulent structures. This study compares certain properties of a 2.5-dimensional particle-in-cell (PIC) simulation for the forward cascade of Alfvénic turbulence in a collisionless plasma against the same properties of turbulence observed by the Magnetospheric Multiscale Mission spacecraft in the terrestrial magnetosheath. The PIC simulation is of decaying turbulence that develops both coherent structures and anisotropic ion velocity distributions with the potential to drive kinetic scale instabilities. The uniform background magnetic field points perpendicular to the plane of the simulation. Growth rates are computed from linear theory using the ion temperature anisotropies and ion beta values for both the simulation and the observations. Both the simulation and the observations show that strong anisotropies and growth rates occur highly intermittently in the plasma, and the simulation further shows that such anisotropies preferentially occur near current sheets. This suggests that, though microinstabilities may affect the plasma globally, they act locally and develop in response to extreme temperature anisotropies generated by turbulent structures. Further studies will be necessary to understand why there is an apparent correlation between linear instability theory and strongly intermittent turbulence.

Unified Astronomy Thesaurus concepts: Space plasmas (1544); Magnetohydrodynamical simulations (1966)

1. Introduction

The magnetized plasma of the solar wind is heated and accelerated in the solar corona, from which it flows continuously and supersonically into deep space. Earth’s magnetic field obstructs and deflects part of this flow, which results in a region of subsonic solar plasma known as the magnetosheath.

The low density and extreme dynamics of space plasmas such as these ensure that they almost invariably deviate substantially from local thermal equilibrium (Marsch 2006; Verscharen et al. 2019). For example, even though the majority of solar wind ions are protons (ionized hydrogen) or α -particles (fully ionized helium), these two particle species rarely have equal temperatures or bulk velocities (see, e.g., Feldman et al. 1974a; Marsch et al. 1982a; Hefti et al. 1998; Kasper et al. 2008; Maruca et al. 2013). Furthermore, the velocity distribution function (VDF) of any given ion species often significantly departs from the entropically favored Maxwellian condition functional form (Feldman et al. 1973a, 1974b; Marsch et al. 1982b; Alterman et al. 2018).

The study described herein focuses on protons and, in particular, on their temperature–anisotropy: a phenomenon where the VDF lacks spherical symmetry. Observations of

solar wind and the magnetosheath from multiple spacecraft (Feldman et al. 1973b; Marsch et al. 1982b; Kasper et al. 2002) have shown that the core of proton VDFs can often be approximated as ellipsoidal and aligned with the plasma’s local magnetic field, \mathbf{B}_0 . Consequently, the protons exhibit distinct kinetic temperatures, $T_{\perp p}$ and $T_{\parallel p}$, in the directions perpendicular and parallel to \mathbf{B}_0 . Proton temperature anisotropy is commonly quantified by the ratio $R_p \equiv T_{\perp p} / T_{\parallel p}$. Both values of $R_p > 1$ and $R_p < 1$ are commonly observed in the solar wind and in Earth’s magnetosheath.

If R_p departs sufficiently from unity, it can trigger a kinetic microinstability: a short-wavelength fluctuation with an exponentially growing amplitude that is fueled by the VDF’s free energy (see Section 2). The threshold R_p value for the onset of a proton temperature–anisotropy instability depends on all plasma parameters (e.g., composition and relative temperatures) but depends most strongly on proton parallel beta,

$$\beta_{\parallel p} = \frac{n_p k_B T_{\parallel p}}{B_0^2 / (2 \mu_0)}, \quad (1)$$

where n_p is the proton number density, k_B is the Boltzmann constant, and μ_0 is the permeability of free space. A detailed

and comprehensive discussion on linear growth rates, calculation methodology, and threshold values can be found in Gary (1993).

These instabilities have threshold R_p values, which means that they can effectively limit the degree to which the proton temperature can depart from isotropy. If an unstable mode grows and does not saturate, it eventually becomes nonlinear, scatters particles in phase space, and drives the VDF toward local thermal equilibrium. Multiple studies have analyzed large data sets from various spacecraft and under the assumptions of a spatially homogeneous plasma and a bi-Maxwellian proton velocity distribution, such studies have found that the joint distribution of $(\beta_{\parallel p}, R_p)$ values from the interplanetary solar wind largely conforms to the limits set by the instability thresholds (Gary et al. 2001; Kasper et al. 2002; Hellinger et al. 2006; Matteini et al. 2007). A recent study by Maruca et al. (2018) confirmed the same effect in Earth’s magnetosheath. Additional studies have found that plasma with unstable $(\beta_{\parallel p}, R_p)$ values is statistically more likely to exhibit enhancements in magnetic fluctuations (Bale et al. 2009) and the proton temperature (Maruca et al. 2011). These findings suggest that the instabilities not only regulate temperature anisotropy in space plasmas but, in doing so, play an integral role in the large-scale evolution of the plasmas.

Despite these extensive statistical studies, relatively little attention has been devoted to understanding the spatial distribution of the unstable modes within the plasma. The empirical studies of $(\beta_{\parallel p}, R_p)$ distributions—especially that by Matteini et al. (2007)—indicate that the instabilities globally limit proton temperature anisotropy and affect the large-scale thermodynamics of expanding solar wind plasma. Nevertheless, the instabilities themselves act on far smaller scales. Indeed, Osman et al. (2012a) found that unstable $(\beta_{\parallel p}, R_p)$ values are statistically more likely to exhibit enhanced values of the partial variance of increments (PVI), which is an indicator of an intermittent structure. This result suggests that long-wavelength turbulence may play a substantial role in generating the local plasma conditions that drive these microinstabilities. Also, advancements made in numerical simulation by Servidio et al. (2012, 2015) and Greco et al. (2012), with corroboration from space plasma observations (Marsch et al. 1992; Sorriso-Valvo et al. 1999; Kiyani et al. 2009; Osman et al. 2011, 2012a), show the importance of intermittency in interpretation of these observations.

The question of where these instabilities develop raises the more fundamental issue of reconciling the assumptions of the theory of microinstabilities, which assumes a homogeneous background, with the observed state of space plasma, which is rarely homogeneous. In the theory of microinstability, instability thresholds are computed using linear Vlasov theory. However, multiple studies have shown space plasma to be highly structured and thus inhomogeneous (Burlaga 1968; Tsurutani & Smith 1979; Ness & Burlaga 2001; Greco et al. 2012; Osman et al. 2012a, 2012b). This has been a persistent question in the field and a prime motivation for our work that formalizes the implications of Osman et al. (2012a).

Analyses of both high-resolution kinetic simulation and high-cadence in situ observations reveal that proton temperature–anisotropy instabilities are distributed intermittently in physical space. Section 2 lays the background of linear theory and instability threshold calculations and discusses the underlying inconsistencies. The computed growth rates were used to

interpret both the kinetic simulation and in situ observations, which are discussed in Sections 3 and 4, respectively. Section 5 summarizes the conclusions of this study.

2. Background

2.1. Microinstabilities in Plasma

Linear growth rates are calculated using the linear dispersion relation obtained from the Vlasov equation. Gary (1993) discusses the computation methodology in great detail. We use the value of these growth rates to determine if the plasma VDF in a certain space at a certain time is susceptible to being unstable or not. For this purpose, we set a cutoff for γ_{jp}/Ω_p at 10^{-5} , where γ_{jp} is one of the four microinstability growth rates arising because of proton temperature–anisotropy and Ω_p is the proton–cyclotron frequency. For parallel propagation, we get cyclotron and parallel firehose instability for $R_p > 1$ and $R_p < 1$, respectively. The oblique (non-propagating) modes are mirror for $R_p > 1$ and oblique firehose for $R_p < 1$.

Though linear theory works well for plasma with homogeneous background, when it comes to its application to space plasmas to study the characteristics of space plasmas, the method is not without caveats. Multiple studies have shown space plasma to be highly structured and thus inhomogeneous (Burlaga 1968; Tsurutani & Smith 1979; Ness & Burlaga 2001; Greco et al. 2012; Osman et al. 2012a, 2012b). In fact, by all accounts, inhomogeneity is ubiquitously present in the space plasma, and thus any study of instabilities in plasma should take into account the inhomogeneity of the background among variation in other parameters.

Consequently, use of the linear theory for such studies of course presents a theoretical inconsistency in the application of computed instability thresholds to study the properties of plasma because of the underlying disparity between the assumptions of linear theory and observed space plasma. However, several studies over the last three decades have presented empirical evidence of agreement between the observations and theoretical prediction (Gary 1991; Gary et al. 1994, 2001; Kasper et al. 2002; Gary & Karimabadi 2006; Hellinger et al. 2006; Maruca et al. 2011, 2012, 2018). These studies strongly suggest that linear instability thresholds are indeed efficient in restricting the plasma/plasma VDF in a narrow region of $\beta_{\parallel p}$ – R_p plane inhibiting excursion of plasma VDFs to extreme anisotropy regions at high $\beta_{\parallel p}$. Although limitations on spatial and temporal resolution using present-day spacecraft make it difficult to directly demonstrate the existence of such instabilities in space plasmas, work done by Bale et al. (2009), He et al. (2011), Podesta (2013), Jian et al. (2009, 2010, 2014), Klein et al. (2014), Telsoni & Bruno (2016), Gary et al. (2016), and others provide indirect evidence for the presence of various different instabilities. More details could be found in Verscharen et al. (2019) and references therein.

An ideal study would indeed include the effect of background inhomogeneities in computing the growth rates. However, we do not have any such established methodology and development of such a method is beyond the scope of this study. We thus are restricted to use the established theory of microinstabilities and to calculate instability thresholds from linear Vlasov equations. Although we do not discuss the consequences of electron anisotropies here, we note that both computer simulations and magnetosheath observations (Gary et al. 2005)

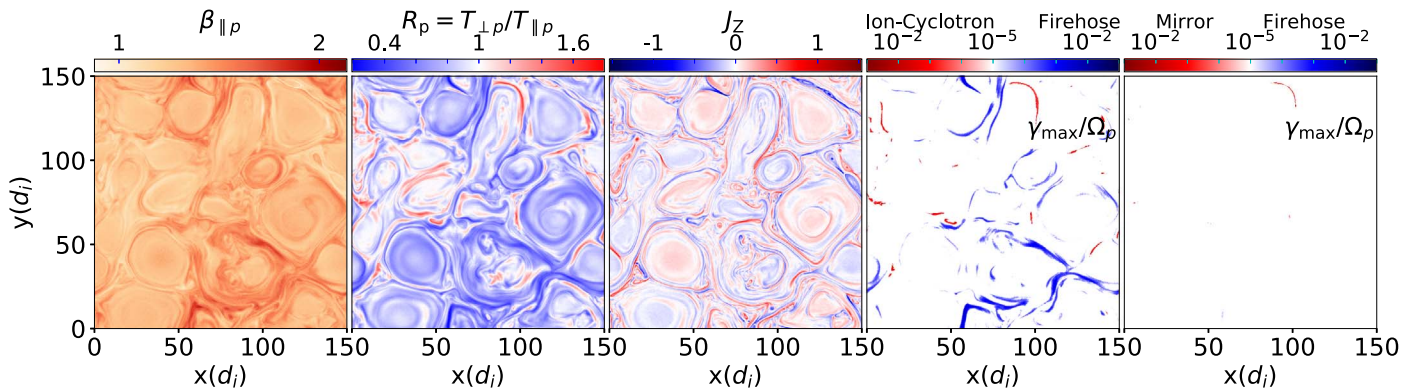


Figure 1. Color plot of (left to right) $\beta_{\parallel p}$, R_p and J_z from a fully kinetic 2.5D PIC simulation with the initial condition of $\beta_p = \beta_e = 1.2$, $T_p = T_e$, and $R_p = 1$. The fourth and fifth panels show the spatial distribution of γ_{\max} for parallel and oblique propagation, respectively, corresponding to first two panels.

have shown that electron temperature anisotropies in collisionless plasmas can drive whistler instabilities that, in turn, scatter the electrons to establish a constraint on the anisotropy of that species (Gary & Wang 1996), which is in full analogy with the case of ion instabilities and anisotropy constraints discussed here.

3. Results: PIC Simulation

We first applied our linear Vlasov calculations to the output of fully kinetic, particle-in-cell (PIC) simulation in homogeneous, collisionless, magnetized plasmas with \mathbf{B}_0 in the z -direction that we implemented with the P3D code (Zeiler et al. 2002). As this was a 2.5D simulation, all vector quantities were modeled as having three components, but all plasma parameters varied only in the xy plane. For this study, the initial conditions were chosen such that the particle distribution was Maxwellian, $\beta_p = \beta_e = 1.2$, $R_p = 1$, $T_p = T_e$, and the rms value of fluctuations in magnetic and velocity fields were half of the background values. High β values as well as values much lower than 1 make the PIC computations very expensive and thus were avoided. The system was then allowed to evolve without any external forcing. Fluctuation in the observed magnetic and velocity fields produce and drive the turbulence in the plasma. All the analyses presented here are performed near the instant at which the mean square of out of plane current (J_z) peaks, when the nonlinear processes are known to be most active. More details about the simulation can be found in Parashar et al. (2018a).

The first three panels of Figure 1 show the three parameters— R_p , $\beta_{\parallel p}$, and J_z —across the simulation box. The system is strongly turbulent and exhibits structures of various scales. The extreme values of each parameter occur in distinct regions that occupy only small fractions of the total volume. That is, these quantities are intermittent, which is correlated with the existence of sharp gradients and coherent structures (Greco & Perri 2014; Matthaeus et al. 2015; Greco et al. 2016; Perrone et al. 2016, 2017). Further, the extreme values of R_p and $\beta_{\parallel p}$ reside near (but not exactly coincident with) the extreme values of J_z . These concentrations of current densities frequently correspond to current sheets, as reported in Parashar & Matthaeus (2016).

Using the method described in Section 2, we computed γ_{\max} for the $(\beta_{\parallel p}, R_p)$ pair at each grid point of the simulation, where γ_{\max} is the maximum value of growth rate for all possible values of the propagation vector (\mathbf{k}). The fourth and fifth panels of Figure 1 show the spatial distribution of growth rates for the solutions with positive growth rates, corresponding to the first

two panels of the same figure. As described in Section 2, for γ_{\max} , we imposed a cutoff at $10^{-5}\Omega_p$; thus, growth rates less than $10^{-5}\Omega_p$ are considered to be 0. The fourth panel of Figure 1 corresponds to the parallel modes (cyclotron for $R_p > 1$ and parallel firehose for $R_p < 1$), whereas the fifth panel is for the oblique propagation (mirror for $R_p > 1$ and oblique firehose for $R_p < 1$). The paucity of the blue in the fifth panel implies that the $\beta_{\parallel p}$ (and/or R_p) was rarely high (low) enough to excite any mode of oblique firehose instability.

Comparing the second panel to the fourth and fifth of Figure 1, we see that values of $\gamma_{\max} > 0$ are concentrated in distinct, filament-like regions of the xy plane where extreme values of temperature anisotropy also occur. We note that, because the simulation is 2.5D with \mathbf{B}_0 perpendicular to the simulation plane, the growth of instabilities, such as the proton-cyclotron and the parallel proton firehose with maximum growth at $\mathbf{k} \times \mathbf{B}_0 = 0$, is suppressed.

4. Results: MMS Observations

We carried out a similar analysis on an interval of burst-mode measurements of the magnetosheath from Magnetospheric Multiscale Mission (MMS).

MMS is a constellation of four identical spacecraft designed to study reconnection in the magnetosphere of the Earth (Burch et al. 2016). We used proton density and temperature-anisotropy data from the Fast Plasma Investigation (FPI) and magnetic field data from the Fluxgate Magnetometer (FGM). In the burst mode, FPI measures one proton distribution every 150 ms (Pollock et al. 2016), and the cadence of FGM is 128 Hz (Russell et al. 2016).

Using the measured temperature-anisotropy and magnetic field vectors, we computed the value of the linear instability growth rates (γ_{\max}) for each point in the time series using the same methodology as described in Section 3. For this analysis, we chose a 40 minute long period of burst data from 2017 December 26 starting at 06:12:43 UTC. This period was chosen in part because of its relatively long duration compared to typical burst-mode intervals. During this period, the average proton density was 22 cm^{-3} , the average value of $\beta_{\parallel p}$ was 4.5, and average bulk velocity of the plasma was 238 km s^{-1} . More details about this particular period can be found in Parashar et al. (2018b).

Figure 2 shows a typical 10 minute portion of the time series of the data discussed above. The panels, from top to bottom,

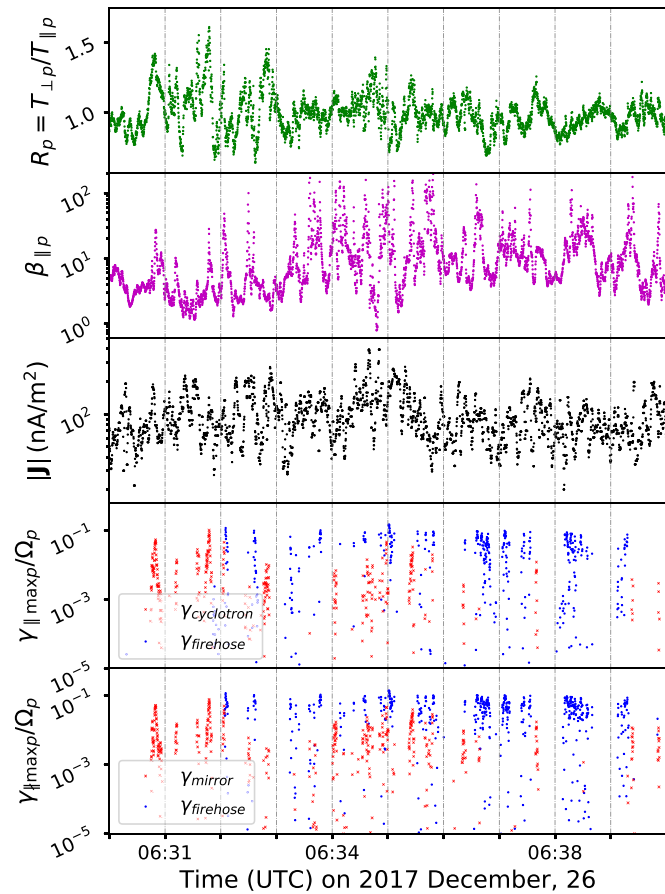


Figure 2. Time series plot of the proton anisotropy ratio (R_p), proton parallel beta ($\beta_{\parallel p}$), total current density in nA m^{-2} , parallel instability growth rates (proton–cyclotron in red and parallel firehose in blue), and oblique instability growth rates (mirror in red and oblique firehose in blue), as observed by MMS on 2017 December 26.

show R_p , $\beta_{\parallel p}$, $|J|$ and maximum growth rates (γ_{\max}) for parallel and oblique instabilities, respectively.

Comparing Figures 1 and 2, we see that a larger fraction the MMS data (30%) are unstable versus grid points from the simulation (0.8%), with γ_{\max} values above the cutoff ($10^{-5}\Omega_p$). This discrepancy arises in part because MMS data have much higher values of $\beta_{\parallel p}$ than the simulation (median values of 4.5 and 1.2, respectively). Furthermore, Servidio et al. (2015) found that, for a given value of $\beta_{\parallel p}$, simulations of the turbulence type, like in the present case, generally admit less extreme temperature–anisotropy than is seen in space observations, because typical simulations are of a modest size and lack large-scale driving.

The time series for MMS observation, (Figure 2) exhibits an intermittent structure in the distribution of growth rates that are similar to what we see in fourth and fifth panels of Figure 1 for the simulation. Figure 3, which shows the comparison of the time series of simulation and MMS data for a 1 minute period, shows that, qualitatively, they have a similar distribution. The time series for the simulation was computed by flying a virtual spacecraft, traveling at the plasma bulk speed (238 km s^{-1}), through the entire box at an angle of 75° with respect to x -direction.

In Figure 2, the points of instabilities ($\gamma_{\max} > 0$) are concentrated together, spreading over a small time interval lasting typically a few seconds (4–8 s) with sharp peaks.

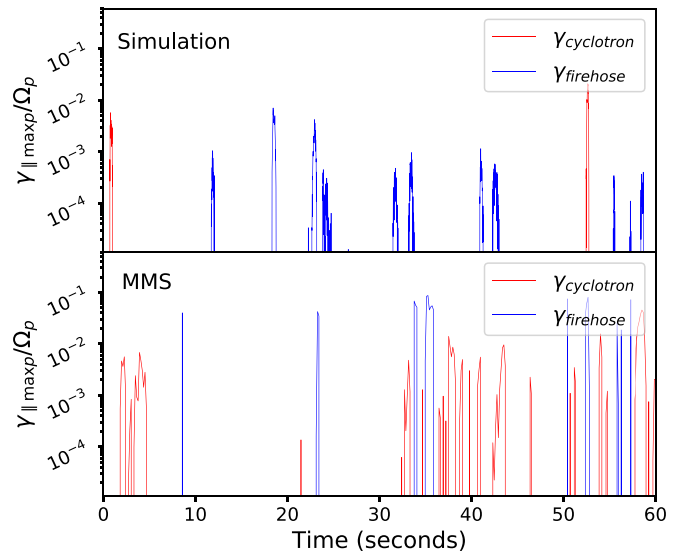


Figure 3. Comparison of simulation and MMS time series for $\gamma_{\parallel \max}$ values for a 1 minute period. The top panel shows the distribution for a 1 minute long flight through the simulation box and the lower panel shows the distribution of γ_{\max} starting at 06:34 on 2017 December 26.

Though, in this study, we did not quantify the length scale of all the peaks, we found that typically they are spread over a length scale of $\sim 20\text{--}40d_i$, where d_i is the ion-inertial length and the length scale was calculated using the flow speed of the plasma and the duration of the peak.

5. Discussion and Conclusion

In recent years, two different perspectives have been widely used to explain the behavior of the solar wind, magnetosheath, and similar space plasmas. In the first picture, the linear theory of plasma instability, at high $\beta_{\parallel p}$, for extreme R_p , different instability thresholds become active, thereby confining the plasma population to lower values of R_p (Gary et al. 2001; Kasper et al. 2002; Hellinger et al. 2006; Matteini et al. 2007; Klein et al. 2018). In the second, turbulence generates sharp gradients in the plasma that produce temperature anisotropy (Osman et al. 2011; Greco et al. 2012; Valentini et al. 2014; Parashar & Matthaeus 2016).

These two theories have been non-reconcilable because of the basic underlying assumption. The linear theory of plasma instability assumes a homogeneous background magnetic field whereas turbulence relies on large fluctuations in the field. It was hitherto unclear if these two seemingly disparate processes—microinstabilities and turbulence—are connected in any way in configuration space. The apparent contradiction—homogeneity against intermittent inhomogeneity—between the two interpretations poses a question of fundamental importance in the study of space plasmas specifically and collisionless plasmas in general: how can an inhomogeneous phenomenon such as turbulence be consistent with anisotropy constraints derived from the linear theory of homogeneous plasmas? Our simulation shows that the turbulence indeed heats the plasma anisotropically. But the simulation also show that these anisotropies are strongly localized; furthermore, the 2.5D character of the simulation with a strong background magnetic field out of the simulation plane acts against the growth of the proton–cyclotron and parallel proton firehose microinstabilities which are the more likely sources of the proton anisotropy

constraints. So it appears that the best we can say now is that at present, we do not understand why there should be a correlation between linear the theory and strongly intermittent turbulence. Clearly, further studies are necessary to resolve this apparent contradiction.

In Figure 1, the regions of significant growth rates are close to the regions of peak current values. This suggests that current sheets are producing the extreme temperature–anisotropies that ultimately drive the instabilities. Note, though, that the high- γ_{\max} regions and the high- J_z regions do not perfectly overlap: they tend to be adjacent to each other rather than co-located, as seen in Greco et al. (2012). Thus, traditional methods of correlation calculation would be inadequate to quantify the relationship between these two structures. Instead, an analysis using cross correlations of these quantities (see e.g., Parashar & Matthaeus 2016) or joint distributions (see e.g., Yang et al. 2017) to explore the causal connection between instabilities and turbulence-generated current sheets would be the next step forward.

In this paper, we have found an explicit connection between intermittency in plasma turbulence and the local enhancement of linear instability growth rates. Intermittency, or burstiness, in measured properties of turbulence is typically associated with the dynamical formation of coherent structures in space. In hydrodynamics, these structures would be found in the vorticity or velocity increments. In the magnetohydrodynamics or plasma context, intermittent structures of other types can be found, such as sheets or cores of electric current density (Biskamp 1986; Carbone et al. 1990). A phenomenology of intermittent plasma structures has begun largely due to advances in numerical simulation (e.g., Greco et al. 2012; Servidio et al. 2012, 2015) with confirmation and guidance emerging from observations in space (Marsch et al. 1992; Horbury et al. 1997; Sorriso-Valvo et al. 1999; Kiyani et al. 2009; Osman et al. 2011, 2012a). Intermittency is clearly influential in the interpretation of observations, while its theoretical importance derives from its potential connection to the nature and statistics of dissipation (Kolmogorov 1962; Karimabadi et al. 2013; Howes 2015; Matthaeus et al. 2015; Wan et al. 2016). The connection we have found here—that linear instability growth rates computed from (admittedly oversimplified) homogeneous plasma theory also occur in intermittent bursts—adds to this emerging understanding of plasma dissipation. Previous studies found that pathways, such as inertial range transfer (Sorriso-Valvo et al. 2019), electromagnetic work (Wan et al. 2012), electron energization (Karimabadi et al. 2013), and pressure-strain interactions (Yang et al. 2017) concentrate in small sub-volumes of plasma turbulence. Dynamical processes that lead to dissipation, such as magnetic reconnection, also occur in spatially localized regions (Drake et al. 2008). Along with these, we now have seen that velocity-space driven phenomena (Greco et al. 2012; Servidio et al. 2012, 2015; Schekochihin et al. 2016) also occur in similar highly localized sub-volumes. The nature of the spatial or regional correlations of these kinetic processes to the surrounding dynamical processes that drive them largely remains to be explored.

T.N.P. was supported by NSF SHINE grant AGS-1460130 and NASA HGI grant 80NSSC19K0284. W.H.M. is a member of the MMS Theory and Modeling Team and was supported by





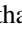



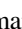





NASA grant NNX14AC39G. The research of S.P.G. was supported by NASA grant NNX17AH87G.

This study used Level 2 FPI and FIELDS data according to the guidelines set forth by the MMS instrumentation team. All data are freely available at <https://lasp.colorado.edu/mms/sdc/>.

We thank the MMS SDC, FPI, and FIELDS teams for their assistance with this study. We acknowledge high-performance computing support from Cheyenne (<https://www2.cisl.ucar.edu/resources/computational-systems/cheyenne>) provided by NCAR’s Computational and Information Systems Laboratory, sponsored by the National Science Foundation. These simulations were performed as part of the Accelerated Scientific Discovery Program (ASD).

The author would like to thank Rohit Chibber and Mark Pultrone for their inputs on the draft and several useful discussions.

ORCID iDs

Ramiz A. Qudsi  <https://orcid.org/0000-0001-8358-0482>
 Riddhi Bandyopadhyay  <https://orcid.org/0000-0002-6962-0959>
 Bennett A. Maruca  <https://orcid.org/0000-0002-2229-5618>
 Tulasi N. Parashar  <https://orcid.org/0000-0003-0602-8381>
 William H. Matthaeus  <https://orcid.org/0000-0001-7224-6024>
 Alexandros Chasapis  <https://orcid.org/0000-0001-8478-5797>
 S. Peter Gary  <https://orcid.org/0000-0002-4655-2316>
 Barbara L. Giles  <https://orcid.org/0000-0001-8054-825X>
 Daniel J. Gershman  <https://orcid.org/0000-0003-1304-4769>
 Craig J. Pollock  <https://orcid.org/0000-0001-9228-6605>
 Robert J. Strangeway  <https://orcid.org/0000-0001-9839-1828>
 Roy B. Torbert  <https://orcid.org/0000-0001-7188-8690>
 Thomas E. Moore  <https://orcid.org/0000-0002-3150-1137>
 James L. Burch  <https://orcid.org/0000-0003-0452-8403>

References

- Alterman, B. L., Kasper, J. C., Stevens, M. L., & Koval, A. 2018, *ApJ*, **864**, 112
- Bale, S. D., Kasper, J. C., Howes, G. G., et al. 2009, *PhRvL*, **103**, 211101
- Biskamp, D. 1986, *PhFl*, **29**, 1520
- Burch, J. L., Moore, T. E., Torbert, R. B., & Giles, B. L. 2016, *SSRv*, **199**, 5
- Burlaga, L. F. 1968, *SoPh*, **4**, 67
- Carbone, V., Veltri, P., & Mangeney, A. 1990, *PhFIA*, **2**, 1487
- Drake, J. F., Shay, M. A., & Swisdak, M. 2008, *PhPl*, **15**, 042306
- Feldman, W. C., Asbridge, J. R., & Bame, S. J. 1974a, *JGR*, **79**, 2319
- Feldman, W. C., Asbridge, J. R., Bame, S. J., & Montgomery, M. D. 1973a, *JGR*, **78**, 2017
- Feldman, W. C., Asbridge, J. R., Bame, S. J., & Montgomery, M. D. 1973b, *JGR*, **78**, 6451
- Feldman, W. C., Asbridge, J. R., Bame, S. J., & Montgomery, M. D. 1974b, *RvGSP*, **12**, 715
- Gary, S. P. 1991, *SSRv*, **56**, 373
- Gary, S. P. 1993, *Theory of Space Plasma Microinstabilities* (Cambridge: Cambridge Univ. Press)
- Gary, S. P., Anderson, B. J., Denton, R. E., Fuselier, S. A., & McKean, M. E. 1994, *PhPl*, **1**, 1676
- Gary, S. P., Jian, L. K., Broiles, T. W., et al. 2016, *JGRA*, **121**, 30
- Gary, S. P., & Karimabadi, H. 2006, *JGRA*, **111**, A11224
- Gary, S. P., Lavraud, B., Thomsen, M. F., Lefebvre, B., & Schwartz, S. J. 2005, *GeoRL*, **32**, L13109
- Gary, S. P., Skoug, R. M., Steinberg, J. T., & Smith, C. W. 2001, *GeoRL*, **28**, 2759
- Gary, S. P., & Wang, J. 1996, *JGRA*, **101**, 10749

- Greco, A., & Perri, S. 2014, *ApJ*, **784**, 163
- Greco, A., Perri, S., Servidio, S., Yordanova, E., & Veltri, P. 2016, *ApJL*, **823**, L39
- Greco, A., Valentini, F., Servidio, S., & Matthaeus, W. H. 2012, *PhRvE*, **86**, 066405
- He, J., Marsch, E., Tu, C., Yao, S., & Tian, H. 2011, *ApJ*, **731**, 85
- Hefü, S., Grünwaldt, H., Ipavich, F. M., et al. 1998, *JGR*, **103**, 29697
- Hellinger, P., Trávníček, P., Kasper, J. C., & Lazarus, A. J. 2006, *GeoRL*, **33**, L09101
- Horbury, T. S., Balogh, A., Forsyth, R. J., & Smith, E. J. 1997, *AdSpR*, **19**, 847
- Howes, G. G. 2015, *RSPTA*, **373**, 20140145
- Jian, L. K., Russell, C. T., Luhmann, J. G., et al. 2009, *ApJL*, **701**, L105
- Jian, L. K., Russell, C. T., Luhmann, J. G., et al. 2010, *JGRA*, **115**, A12115
- Jian, L. K., Wei, H. Y., Russell, C. T., et al. 2014, *ApJ*, **786**, 123
- Karimabadi, H., Roytershteyn, V., Wan, M., et al. 2013, *PhPI*, **20**, 012303
- Kasper, J. C., Lazarus, A. J., & Gary, S. P. 2002, *GeoRL*, **29**, 20
- Kasper, J. C., Lazarus, A. J., & Gary, S. P. 2008, *PhRvL*, **101**, 261103
- Kiyani, K. H., Chapman, S. C., Khotyaintsev, Y. V., Dunlop, M. W., & Sahraoui, F. 2009, *PhRvL*, **103**, 075006
- Klein, K. G., Alterman, B. L., Stevens, M. L., Vech, D., & Kasper, J. C. 2018, *PhRvL*, **120**, 205102
- Klein, K. G., Howes, G. G., TenBarge, J. M., & Podesta, J. J. 2014, *ApJ*, **785**, 138
- Kolmogorov, A. N. 1962, *JFM*, **13**, 82
- Marsch, E. 2006, *LRSP*, **3**, 1
- Marsch, E., Liu, S., Rosenbauer, H., & Tu, C. Y. 1992, in *ESA SP-346, Study of the Solar-Terrestrial System*, ed. J. J. Hunt (Noordwijk: ESA), 315
- Marsch, E., Mühlhäuser, K.-H., Rosenbauer, H., Schwenn, R., & Neubauer, F. M. 1982a, *JGR*, **87**, 35
- Marsch, E., Schwenn, R., Rosenbauer, H., et al. 1982b, *JGR*, **87**, 52
- Maruca, B., Kasper, J., & Bale, S. 2011, *PhRvL*, **107**, 201101
- Maruca, B. A., Bale, S. D., Sorriso-Valvo, L., Kasper, J. C., & Stevens, M. L. 2013, *PhRvL*, **111**, 241101
- Maruca, B. A., Chasapis, A., Gary, S. P., et al. 2018, *ApJ*, **866**, 25
- Maruca, B. A., Kasper, J. C., & Gary, S. P. 2012, *ApJ*, **748**, 137
- Matteini, L., Landi, S., Hellinger, P., et al. 2007, *GeoRL*, **34**, 20105
- Matthaeus, W. H., Wan, M., Servidio, S., et al. 2015, *RSPTA*, **373**, 20140154
- Ness, N. F., & Burlaga, L. F. 2001, *JGRA*, **106**, 15803
- Osman, K. T., Matthaeus, W. H., Greco, A., & Servidio, S. 2011, *ApJL*, **727**, L11
- Osman, K. T., Matthaeus, W. H., Hnat, B., & Chapman, S. C. 2012a, *PhRvL*, **108**, 261103
- Osman, K. T., Matthaeus, W. H., Wan, M., & Rappazzo, A. F. 2012b, *PhRvL*, **108**, 261102
- Parashar, T. N., Chasapis, A., Bandyopadhyay, R., et al. 2018b, *PhRvL*, **121**, 265101
- Parashar, T. N., & Matthaeus, W. H. 2016, *ApJ*, **832**, 57
- Parashar, T. N., Matthaeus, W. H., & Shay, M. A. 2018a, *ApJL*, **864**, L21
- Perrone, D., Alexandrova, O., Mangeney, A., et al. 2016, *ApJ*, **826**, 196
- Perrone, D., Alexandrova, O., Roberts, O. W., et al. 2017, *ApJ*, **849**, 49
- Podesta, J. J. 2013, *SoPh*, **286**, 529
- Pollock, C., Moore, T., Jacques, A., et al. 2016, *SSRv*, **199**, 331
- Russell, C. T., Anderson, B. J., Baumjohann, W., et al. 2016, *SSRv*, **199**, 189
- Schekochihin, A. A., Parker, J. T., Highcock, E. G., et al. 2016, *JPIPh*, **82**, 905820212
- Servidio, S., Valentini, F., Califano, F., & Veltri, P. 2012, *PhRvL*, **108**, 045001
- Servidio, S., Valentini, F., Perrone, D., et al. 2015, *JPIPh*, **81**, 325810107
- Sorriso-Valvo, L., Carbone, V., Veltri, P., Consolini, G., & Bruno, R. 1999, *GeoRL*, **26**, 1801
- Sorriso-Valvo, L., Catapano, F., Retinò, A., et al. 2019, *PhRvL*, **122**, 035102
- Telloni, D., & Bruno, R. 2016, *MNRAS: Letters*, **463**, L79
- Tsurutani, B. T., & Smith, E. J. 1979, *JGRA*, **84**, 2773
- Valentini, F., Vecchio, A., Donato, S., et al. 2014, *ApJL*, **788**, L16
- Verscharen, D., Klein, K. G., & Maruca, B. A. 2019, *LRSP*, **16**, 5
- Wan, M., Matthaeus, W. H., Karimabadi, H., et al. 2012, *PhRvL*, **109**, 195001
- Wan, M., Matthaeus, W. H., Roytershteyn, V., et al. 2016, *PhPI*, **23**, 042307
- Yang, Y., Matthaeus, W. H., Parashar, T. N., et al. 2017, *PhPI*, **24**, 072306
- Zeiler, A., Biskamp, D., Drake, J. F., et al. 2002, *JGRA*, **107**, 1230